THE ASTROPHYSICAL JOURNAL, 483:414–425, 1997 July 1
© 1997. The American Astronomical Society. All rights reserved. Printed in U.S.A.

PHOTOIONIZATION OF HYDROGEN IN ATMOSPHERES OF MAGNETIC NEUTRON STARS

ALEXANDER Y. POTEKHIN
Ioffe Physical-Technical Institute, 194021, St. Petersburg, Russia; palex@astro.ioffe.rssi.ru

AND

GEORGE G. PAVLOV
Pennsylvania State University, 525 Davey Lab, University Park, PA 16802; pavlov@astro.psu.edu
Received 1996 December 9; accepted 1997 January 30

ABSTRACT

The strong magnetic fields ($B \sim 10^{12}$–10^{13} G) characteristic of neutron stars make all the properties of an atom strongly dependent on the transverse component $K_\perp$ of its generalized momentum. In particular, the photoionization process is modified substantially: (1) threshold energies are decreased as compared with those for an atom at rest, (2) cross section values are changed significantly, and (3) selection rules valid for atoms at rest are violated by the motion so that new photoionization channels become allowed. To calculate the photoionization cross sections, we employ, for the first time, exact numerical treatment of both initial and final atomic states. This enables us to take into account the quasi-bound (autoionizing) atomic states as well as coupling of different ionization channels. We extend the previous consideration, restricted to the so-called centered states corresponding to relatively small values of $K_\perp$, to arbitrary states of atomic motion. We fold the cross sections with the thermal distribution of atoms over $\boldsymbol{K}$. For typical temperatures of neutron star atmospheres, the averaged cross sections differ substantially from those of atoms at rest. In particular, the photoionization edges are strongly broadened by the thermal motion of atoms; this "magnetic broadening" exceeds the usual Doppler broadening by orders of magnitude. The decentered states of the atoms give rise to the low-energy component of the photoionization cross section. This new component grows significantly with increasing temperature above $10^{5.5}$ K and decreasing density below 1 g cm^{-3}, i.e., for the conditions expected in atmospheres of middle-aged neutron stars.

Subject headings: atomic processes — stars: magnetic fields — stars: neutron

1. INTRODUCTION

The thermal surface radiation detected recently from a number of isolated neutron stars (NSs) (see, e.g., Ögelman 1995 for a review) provides valuable information about NS temperatures and radii. This data enables one to trace the thermal history of NSs and to put constraints on the properties of the superdense matter in NS interiors (e.g., Pethick 1992). However, the observed spectra are substantially modified by reprocessing of the thermal radiation in NS atmospheres (Romani 1987). Pavlov et al. (1995, and references therein) have shown that the strong magnetic fields of NSs, $B \sim 10^{12}$–10^{13} G, affect the emergent spectra significantly. In particular, photoabsorption by the strongly magnetized atomic hydrogen gas which presumably covers the NS surface should be taken into account. The magnetic field strongly affects the structure and radiative transitions of the hydrogen atom when the electron cyclotron energy $\hbar\omega_c = \hbar eB/(m_e c)$ is much greater than the Rydberg energy $\mathrm{Ry} = m_e e^4/(2\hbar^2) = 13.6$ eV, i.e., $\gamma = \hbar\omega_c/(2\ \mathrm{Ry}) = B/(2.35 \times 10^9\ \mathrm{G}) \gg 1$. In particular, the atom becomes stretched along the magnetic field, the ionization potential is increased by a factor of $\sim(\ln\gamma)^2$, and radiative transition probabilities become strongly dependent on the photon polarization.

Photoionization of strongly magnetized hydrogen atoms *at rest* has been considered by a number of authors. The most thorough consideration in the *adiabatic approximation*, applicable for very large γ and $\omega \ll \omega_c$ (ω is the photon frequency), was presented by Potekhin & Pavlov (1993; hereafter PP93). This approximation neglects coupling of states with different values of the Landau quantum number n, which specifies the energy of the electron motion transverse to the magnetic field (the other quantum number associated with the transverse motion, the projection s of the angular momentum onto the field, is exact for atoms at rest). Potekhin, Pavlov, & Ventura (1997; hereafter PPV97) went beyond the adiabatic approximation and resolved, in particular, a long-standing contradiction: some authors (e.g., Schmitt et al. 1981; Wunner et al. 1983; Ventura et al. 1992) had concluded that the photoionization cross section is exactly zero for photons polarized transversely to the magnetic field, whereas other authors (e.g., Gnedin, Pavlov, & Tsygan 1974; Miller & Neuhauser 1991; PP93) obtained finite cross sections. PP93 showed that the discrepancy was rooted in the use of different forms of the interaction potential (the so-called "velocity form" and the "length form") by the two groups of authors, and PPV97 proved that the velocity form used by the former group resulted in neglecting the main contribution to the cross section. The nonadiabatic approach enabled PPV97 to study correlation of different ionization channels and manifestation of autoionization (Beutler-Fano) resonances in the photoabsorption spectra.

The above-cited papers did not take into account the atomic motion inevitable in any real example of the problem. If there were no strong magnetic field, the motion would only lead to the trivial Doppler broadening of the spectral lines and photoionization edges. On the other hand, finite atomic velocities in strong magnetic fields lead to many qualitatively new effects (Pavlov & Mészáros 1993;

hereafter PM93) associated with strong distortion of the atomic structure by the Lorentz electric field generated by the motion. Since the moving atom loses its cylindrical symmetry, the projection s of the angular momentum is no longer a good quantum number (in other words, the s-adiabatic approach which neglects coupling of states with different s becomes invalid). Hence, the selection rules for the radiative transitions are changed so that new types of transitions become allowed. Since the atomic structure depends on the velocity of the atom, and different atomic states are affected by the motion differently, a new type of broadening of spectral features, *magnetic broadening*, becomes the most important effect.

The energies and wave functions of the moving atom depend on the transverse component $K_\perp$ of a *generalized momentum* $\boldsymbol{K}$ (see below), which, unlike the canonical and kinetic momenta, is conserved for a neutral atom moving in a magnetic field. PM93 analyzed various effects of the motion of the hydrogen atom in the perturbative regime, when $K_\perp$ is small. When $K_\perp$ exceeds some critical value, the magnetic and (motion-generated) electric fields form a potential well at a distance $r_c = m_e K_\perp/\omega_c$ from the proton, which gives rise to so-called *decentered* (or shifted) states (Burkova et al. 1976). The decentered states recover the cylindrical symmetry (s becomes a good quantum number again at large $K_\perp$), but the axis of symmetry, with respect to which s is defined, is shifted by r_c. In other words, these states can be described in the *shifted* s–adiabatic approximation. Binding energies, wave functions and oscillator strengths of radiative transitions between the discrete levels of an arbitrarily moving H atom (beyond the adiabatic approximation) have been studied by Potekhin (1994; hereafter P94). Our recent study of the hydrogen bound-bound opacity in NS atmospheres (Pavlov & Potekhin 1995; hereafter PP95) was based on these results.

The effects of the motion across the field on the bound-free radiative transitions of atoms have been investigated less extensively. PM93 have shown, in the perturbation approach, that the motion strongly affects photoionization cross sections through opening and enhancement of additional photoionization channels forbidden for the nonmoving atom because of its cylindrical symmetry and through the strong magnetic broadening of the photoionization edges. Bezchastnov & Potekhin (1994; hereafter BP94) suggested a modification of the adiabatic approach that allows for different displacements of the initial and final states and presented a convenient formalism for calculating the transition rates between such states. They have also performed calculations with the initial state treated nonadiabatically; the two approaches exhibited a fair agreement with each other. Kopidakis, Ventura, & Herold (1996; hereafter KVH96) also went beyond the perturbation approximation and calculated the frequency dependences of the cross sections for various values of $K_\perp$, assuming these values small enough to neglect the decentered bound states. The results of the two latter papers differ from each other by orders of magnitude for radiation polarized *transversely* to the field. The origin of the discrepancy is the same as for atoms at rest—KVH96 employed the velocity form of the interaction potential, which led to wrong results when used with the n-adiabatic approximation which treats the Landau number n as the exact quantum number. Both BP94 and KVH96 treated final (continuum) states of electron in the (shifted) adiabatic approximation, neglecting coupling of final states with different s and contribution of quasi-bound (autoionizing) states to the photoionization cross section.

The general nonadiabatic numerical approach developed by PPV97 to study the continuum wave functions of the strongly magnetized hydrogen was applied there to the particular case of nonmoving atoms. In the present work, we employ that approach, together with the theoretical formalism of P94 and BP94, for an accurate treatment of both discrete and continuum states of the moving atom and the radiative transitions between them. Unlike BP94 and KVH96, we do not restrict ourselves to the case of relatively small generalized momenta of atoms, but consider also the decentered states that arise at large $K_\perp$. This generality enables us to calculate the cross sections of photoionization by arbitrarily polarized photons of the hydrogen atom arbitrarily moving in a magnetic field of $B \sim 10^{12}$–10^{13} G. Averaging these cross sections with thermal distributions of atoms yields the bound-free opacities needed for modeling NS atmospheres.

In § 2 we outline basic techniques for numerical treatment of a strongly magnetized H atom and its interactions with radiation (the general form of the interaction matrix elements is given in the Appendix). In § 3 we present the photoionization cross sections of H atoms in various states of motion across the magnetic field and cross sections averaged over thermal motion for conditions typical for atmospheres of isolated NSs.

2. THEORETICAL FRAMEWORK

2.1. *Generalized Momentum and Decentering of H Atoms*

The center-of-mass motion of an atom in a magnetic field can be conveniently described by the generalized momentum $\boldsymbol{K}$ (Gorkov & Dzyaloshinskii 1968; see also Johnson, Hirschfelder, & Yang 1983),

$$\boldsymbol{K} = \boldsymbol{P} - \frac{e}{2c}\,\boldsymbol{B} \times (\boldsymbol{r}_e - \boldsymbol{r}_p)\,, \tag{1}$$

where $\boldsymbol{P}$ is the canonical momentum, $\boldsymbol{r}_e - \boldsymbol{r}_p$ is the relative coordinate (the subscript "e" or "p" indicates electron or proton, respectively), and the cylindrical gauge of the vector potential is used. We shall consider the representation in which all three components of $\boldsymbol{K}$ have definite values. Then the two-body wave function can be factorized into a phase factor depending on the center-of-mass coordinate and the wave function $\psi_{\boldsymbol{K}}$ depending on $\boldsymbol{r}_e - \boldsymbol{r}_p$.

It is useful to define a basic electron-proton separation $\eta\boldsymbol{r}_c$ and to regard the deviation from it, $\boldsymbol{r} = \boldsymbol{r}_e - \boldsymbol{r}_p - \eta\boldsymbol{r}_c$, as an independent variable. Here $\boldsymbol{r}_c = (c/eB^2)\boldsymbol{B} \cdot \boldsymbol{K}$ is the position of the relative guiding center and η is the *shift parameter*. It is also convenient to use a special axial gauge of the vector potential (Vincke, Le Dourneuf, & Baye 1992; P94). Then we arrive at a set of Hamiltonians $H^{(\eta)}$ and wave functions $\psi^{(\eta)}(\boldsymbol{r})$ depending on η. In the particular cases of $\eta = 0$ and $\eta = 1$, the "conventional" and "shifted" representations of Gorkov & Dzyaloshinskii (1968) are recovered. Wave functions with different η are related to each other by the phase transformation (BP94)

$$\psi^{(\eta)}_{\boldsymbol{K}}(\boldsymbol{r}) = \exp\left[-\frac{i}{\hbar}\,\frac{m_p - m_e}{2m_{\rm H}}\,\eta\boldsymbol{K}\cdot\boldsymbol{r}_\perp\right]\psi^{(0)}_{\boldsymbol{K}}(\boldsymbol{r} + \eta\boldsymbol{r}_c)\,, \tag{2}$$

where $\boldsymbol{r}_\perp = (x, y)$ is the coordinate transverse to the field $\boldsymbol{B}$ and $m_H = m_e + m_p$ is the total mass of the atom.

If there were no Coulomb attraction, then the electron Landau number $n = 0, 1, 2, \ldots$ and the z-projection of the angular momentum of the relative motion $s \geq -n$ would be exact quantum numbers. In this case the energy of the transverse motion (with the constant minimum energy subtracted) is

$$E_{ns}^{\perp} = [n + (m_e/m_p)(n + s)]\hbar\omega_c \tag{3}$$

and the transverse part of the wave function can be described (for a given $\boldsymbol{K}_\perp$) by a Landau function

$$\Phi_{ns}(\boldsymbol{r}'_\perp) = \frac{1}{a_m\sqrt{2\pi}}\, e^{-is\phi} I_{n+s,n}\left(\frac{r'^2_\perp}{2a_m^2}\right), \tag{4}$$

which depends on $\boldsymbol{r}'_\perp = \boldsymbol{r}_{e\perp} - \boldsymbol{r}_{p\perp} - \boldsymbol{r}_c$ [$= \boldsymbol{r}_\perp(\eta = 1)$]. Here ϕ is the azimuthal angle of $\boldsymbol{r}'_\perp$, $a_m = (\hbar c/eB)^{1/2}$ is the magnetic length, $I_{nn'}$ is a Laguerre function (Sokolov & Ternov 1968), and the z-projection s of the angular momentum of the relative motion is defined in the shifted reference frame, $\eta = 1$ (since $\boldsymbol{K}_\perp$ is definite, the electron and proton do not possess definite z-projections of the angular momenta separately from each other—see Johnson et al. 1983). Equation (4) implies that after photoionization of a moving hydrogen atom, when the photoelectron moves away to large distances at which the Coulomb interaction can be neglected, it acquires the displacement $\boldsymbol{r}_c$ from the proton in the transverse plane.

2.2. *Atomic Wave Functions*

A wave function $\psi_\kappa^{(\eta)}$ of an atomic state $|\kappa\rangle$ can be expanded over the complete set of Landau functions

$$\psi_\kappa^{(\eta)}(\boldsymbol{r}) = \sum_{ns} \Phi_{ns}(\boldsymbol{r}_\perp) g_{n,s;\kappa}^{(\eta)}(z) \tag{5}$$

(note that $\boldsymbol{r}_\perp$ depends on η). The adiabatic approximation corresponds to retaining only one term in this expansion.

A *bound state* of the atom can be numbered as $|i\rangle = |n_i, s_i, v, K\rangle$, where n_i and s_i relate to the leading term of expansion (5) and v enumerates longitudinal energy levels

$$E_i^{\parallel} = E_i - E_{n_i s_i}^{\perp} \tag{6}$$

and controls the z-parity: $g_{n,s;\kappa}^{(\eta)}(-z) = (-1)^v g_{n,s;\kappa}^{(\eta)}(z)$. For a moving atom, this way of numbering is unambiguous at $\gamma \gtrsim 300$ (P94).

Since the transverse factors Φ_{ns} in equation (5) are known analytically, only the one-dimensional longitudinal functions $g_{ns;\kappa}^{(\eta)}$ are to be found numerically. For the bound states, numerical calculations (Vincke et al. 1992; P94) yield the following. At small transverse generalized momenta $K_\perp$, the states $v = 0$ remain tightly bound and *centered*, with the electron cloud concentrated around the proton. For such states, the conventional representation ($\eta = 0$) is appropriate. At large $K_\perp$, the states are *decentered*, with the electron localized in a potential well shifted apart from the proton. Then $\eta = 1$ is the apt choice. With growing $K_\perp$, the transition from the centered tightly-bound states to the decentered states occurs in a narrow range of $K_\perp$ near $K_c \simeq (2m_H|E^{\parallel}|)^{1/2}$, and the shifted ($\eta = 1$) adiabatic approximation becomes fairly good at $K_\perp \gg K_c$. For the hydrogen-like states $v \geq 1$, however, the mean electron-proton separation grows steadily, being close to r_c at arbitrarily small $K_\perp$, so that these states can be described by the shifted adiabatic approximattion at any $K_\perp$. Finally, at very large $K_\perp$ ($\gg \gamma\hbar/a_B$, where a_B is the Bohr radius) the longitudinal functions become oscillator-like for any states, corresponding to a wide, shallow parabolic potential well of a depth $\simeq e^2/r_c$ below the continuum boundary (Burkova et al. 1976; P94).

A *continuum state* can be numbered as $|f\rangle = |n_f, s_f, E_f, I, \boldsymbol{K}'\rangle$, where n_f and s_f correspond to an open channel for the energy E_f and $I = \pm 1$ corresponds to a type of the final state, e.g., to a given z-parity or to a direction of electron escape, depending on asymptotic conditions. In the photoionization process the value of $\boldsymbol{K}'$ is constrained by the momentum conservation law $\boldsymbol{K}' = \boldsymbol{K} + \hbar\boldsymbol{q}$, where $\boldsymbol{q}$ is the photon wavevector.

For the continuum without motion ($K'_\perp = 0$), a technique for calculating the longitudinal wave functions has been developed by PPV97. It can be easily extended to the general case, $K'_\perp \neq 0$, by enumerating the orbitals (n, s) in equation (5) for the state $|f\rangle$ with single integers j such that larger values of j correspond to higher energies $E_{ns}^{\perp}$. Since the Coulomb interaction ceases to distort the transverse wave functions at infinity, the orbitals in equation (5) become uncoupled at large z, provided that the full-shift representation ($\eta' = 1$) of the continuum state is chosen. We shall adopt this choice hereafter.

2.3. *Interaction with Radiation*

The cross section for ionization of an atomic state $|i\rangle$ into a continuum state $|f\rangle$ by a photon with frequency ω, wavevector $\boldsymbol{q}$, and polarization vector $\boldsymbol{e}$ is

$$\sigma_{i\to f} = \pi\,\frac{e^2}{\hbar c}\,\frac{\mathrm{Ry}}{\hbar\omega}\left(\frac{\mathrm{Ry}}{E_f^{\parallel}}\,\frac{\mu}{m_e}\right)^{1/2} L_z\, a_B\, |\langle f|\hat{M}|i\rangle|^2\,, \tag{7}$$

where μ is the reduced mass, L_z is the z-extension of the periodicity volume of the final state, and $\hat{M}$ is the dimensionless interaction operator. For an arbitrarily moving atom of finite mass, the expression for $\hat{M}$ is given in the Appendix. Using equation (5) for both the initial and the final atomic states, we obtain

$$\langle f|\hat{M}|i\rangle = \sum_{nsn's'} \langle n's'\eta', f|\langle n's'\eta'|\hat{M}|ns\eta\rangle_\perp |ns\eta, i\rangle_\parallel\,, \tag{8}$$

where $|ns\eta, \kappa\rangle_\parallel$ corresponds to the longitudinal wave function $g_{ns;\kappa}^{(\eta)}(z)$ and $|ns\eta\rangle_\perp$ corresponds to Φ_{ns}. The interaction operator $\hat{M}$ in this equation depends on η' and η because it includes the common phase factor from eq. (2) (see the Appendix).

The Landau functions for the initial and final states in equation (8) depend on differently displaced arguments if $\eta' \neq \eta$. This case holds for the tightly bound initial states at $K_\perp < K_c$, for which the apt choice of the shift parameter is $\eta = 0$ (while $\eta' = 1$). The different displacements strongly complicate explicit integration in the inner (transverse) matrix elements.

In order to reduce the initial and final wave functions in the same basis, KVH96 expressed the displaced Landau state as a series over the undisplaced states. This reexpansion involves an additional summation index which runs over a huge number of values if the relative displacement is large enough, which renders the reexpansion method impractical at high $K_\perp$.

The difficulty can be circumvented using the creation/annihilation operator formalism of BP94. Analytical calcu-

lation of $\langle n's'\eta' | \hat{M} | ns\eta \rangle_\perp$ is performed in the Appendix. As a result, the interaction matrix element $\langle f | \hat{M} | i \rangle$ reduces to a sum of one-dimensional quadratures (eq. [A9]) feasible for numerical evaluation.

3. RESULTS AND DISCUSSION

3.1. *Photoionization at Fixed $K_\perp$*

Many properties of the photoionization cross section can be understood from the $K_\perp$-dependence of the level energies shown in Figure 1. The monotonic increase of the energies shifts the photoionization thresholds redward. Admixture of many orbitals near "anticrossings" of levels belonging to different s-manifolds (e.g., at $K_\perp \approx 150$ a.u.) causes peculiarities in the radiative transition rates (P94). The levels that lie above zero in Figure 1 correspond to quasi-bound states in the continuum. These levels give rise to sharp resonances in the cross sections at the photon energies corresponding to transitions between the initial bound state and the quasi-bound states.

Figure 2 demonstrates a comparison of our numerical results (*solid lines*) with those obtained using approximations encountered in literature. The dot–short-dashed curves are obtained using the velocity form of the interaction operator with the s'-coupling "switched off" (s'-adiabatic approximation). We see that this coupling is very important for evaluating the cross section σ_- (for the left circular polarization transverse to the magnetic field) and less important for the other two basic cross sections, σ_+ (right circular polarization transverse to the field) and $\sigma_\parallel$ (linear polarization along the field). The dotted lines are obtained using the shifted adiabatic approximation for the final state and the length representation of the interaction operator. Note that they are close to the dot–short-dashed lines in the upper panels. This result is in accordance with the approximate equivalence of the length form with the n-adiabatic approximation (n, $n' = 0$) to the velocity form with allowance for n, $n' > 0$. This equivalence was suggested by PP93 and was proven by PPV97 under the condition that the nonadiabatic corrections are small. The equivalence fails for $K_\perp \sim K_c$ if the s'-coupling is neglected (compare the dotted and dot–short-dashed curves in the bottom panels), but we have checked numerically that it holds if the s, s'-coupling is included.

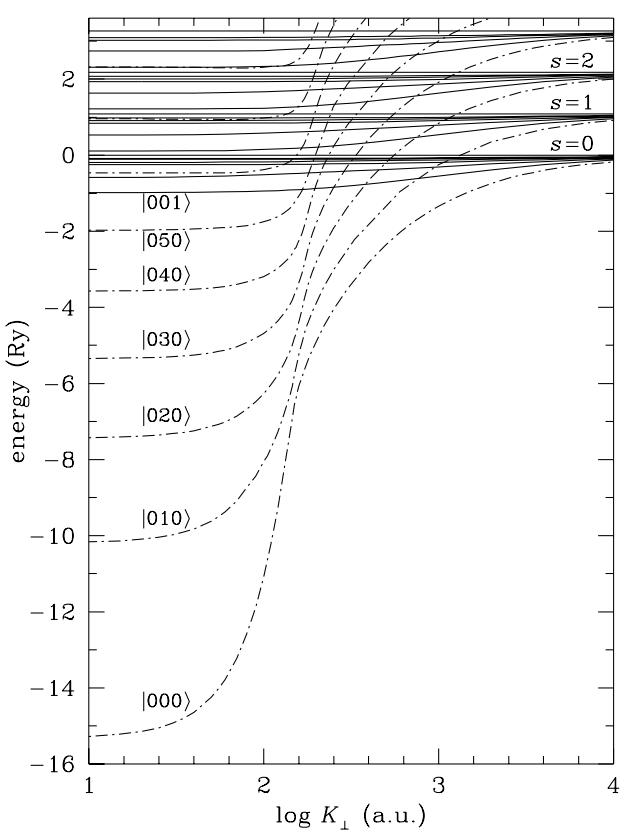

FIG. 1.—Energy spectrum ($E_{0sv} - E_{00}^\perp$) vs. transverse generalized momentum $K_\perp$ at $B = 2.35 \times 10^{12}$ G. The curves (*dot-dashed*, tightly-bound states; *solid*, hydrogen-like states) are labeled with the quantum numbers $|0sv\rangle$.

The dot–long-dashed curves correspond to the approach of BP94, which differs from the plain shifted (n', s')–adiabatic approximation (*dotted curves*) by employing the orthogonalization of the final state with respect to the initial one (see eq. [32] of BP94). At relatively small $K_\perp$ (*upper panels*), this approximation yields qualitatively correct results. With increasing $K_\perp$, the approximate σ_+ becomes progressively less accurate because of violation of the cylindrical symmetry of the continuum states of the atom; for instance, it exceeds our cross section by a factor of ~ 5–7 at $K_\perp = 100$ a.u. However, the approximate σ_- and $\sigma_\parallel$ remain surprisingly accurate.

The short-dashed lines correspond to the approach of KVH96, who use the n-adiabatic approximation for the initial state, and the shifted adiabatic and Born approximations for the final state. If the Born approximation is abandoned (retaining the adiabatic approximation), $\sigma_\pm$ becomes considerably lower, by 0.5 to 3 orders of magnitude for the parameters chosen in Figure 2, making it even more different from the true cross sections. This lowering is due to the approximate orthogonality of the initial and final *longitudinal* wave functions, which is not provided by the Born approximation.

All the approximations discussed fail to produce the Beutler-Fano resonances (narrow peaks and dips near the thresholds) that occur at the energies of the quasi-bound states in the continuum. These resonances are analogous to those discussed by PPV97, except that now these quasi-bound states all belong to the ($n' = 0$)-manifold. Autoionization in this case becomes possible because of the motion-induced coupling of different s'-channels. Except for the missing resonances, the discussed approximations appear to be sufficiently accurate for the longitudinal ($\sigma_\parallel$) polarization.

Figure 3 demonstrates a representative sample of our numerical results for $\gamma = 1000$. In accordance with Figure 1, the photoionization thresholds shift redward with increasing $K_\perp$. Since $K_c \approx 150$ a.u. at this field strength, the left and right panels correspond to the centered and decentered atoms, respectively.

For the centered atoms, the slopes of the curves for each given polarization remain practically coincident with those at $K_\perp = 0$. The values of the cross sections for the parallel and right polarizations, corresponding to the radiative transitions with $s' = s$ and $s' = s + 1$ allowed at $K_\perp = 0$ (when s is a "good" quantum number), decrease only slightly with increasing $K_\perp$ from 0 to K_c. For the left polarization, radiative transitions from the ground state are forbidden ($\sigma_- = 0$) at $K_\perp = 0$ (PP93). With growing $K_\perp$, the coupling between different s-channels increases and σ_- grows

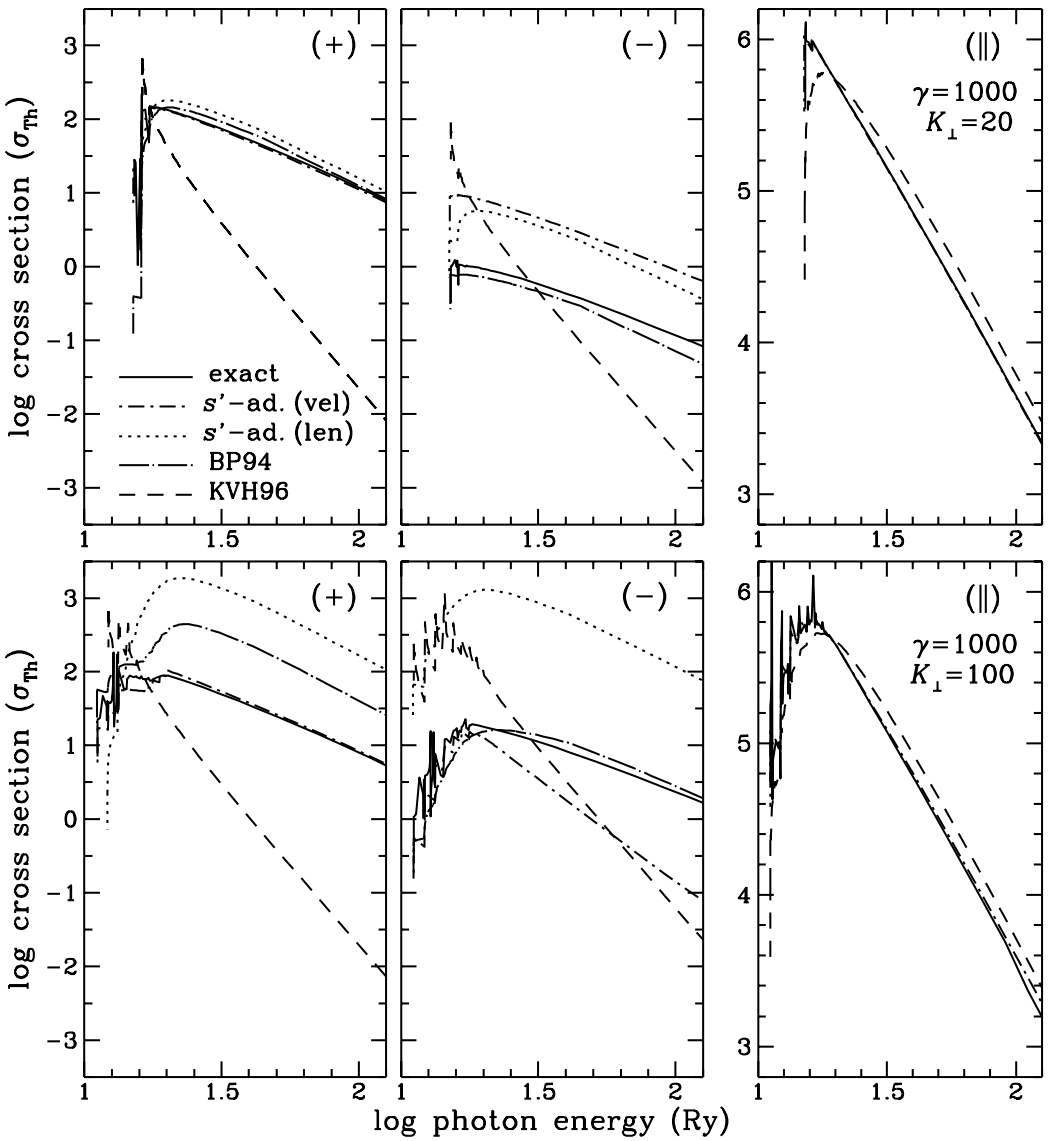

FIG. 2.—Energy dependence of the photoionization cross section (in units of the Thomson cross section $\sigma_{\rm Th}$) of the ground-state H atom moving across the magnetic field $B = 2.35 \times 10^{12}$ G with generalized momentum $K_\perp = 20$ a.u. $\{\kappa \equiv K_\perp a_m/[\hbar(2)^{1/2}] = 0.447$, *top*$\}$ or $K_\perp = 100$ a.u. ($\kappa = 2.236$, *bottom*) for the right (+), left (−), and longitudinal (||) polarizations (the incident photons move along the magnetic field in the former two cases, and across the field in the latter case). Our numerical results (*solid lines*) are compared with several common approximations (see text).

(approximately as $K_\perp^2$; see PM93) until it becomes comparable to σ_+ at $K_\perp \sim K_c$.

For the *decentered* atoms (*right*, Fig. 3), the energy dependences steepen with growing $K_\perp$. This effect is explained by the change of the form of the effective potential from Coulomb-like at $K_\perp \lesssim K_c$ to oscillator-like as the atom becomes decentered. The effective potentials corresponding to different s become nearly identical, which results in a significant decrease of σ_+. The decrease of σ_-, caused by the return to applicability of the s-adiabatic approximation and the corresponding enforcement of selection rules at large $K_\perp$, is even faster. At the same time, the threshold value of $\sigma_\parallel$ remains almost independent of $K_\perp$.

Since the moving atom loses its cylindrical symmetry, the cross sections depend on the angle φ between $\boldsymbol{K}_\perp$ and the transverse component of the wavevector. The φ-dependence is most pronounced when both the wavevector $\boldsymbol{q}$ and the polarization direction $\boldsymbol{e}$ are perpendicular to $\boldsymbol{B}$. The cross sections $\sigma_\parallel$ and $\sigma_\perp$ are shown in Figure 3 as dot–long-dashed and dashed lines, respectively. The former cross section does not depend on φ in the dipole approximation, whereas the small nondipole corrections (eq. [A10c]) cause a weak dependence on φ with an amplitude $\ll 1\%$. Therefore we show only one curve for $\sigma_\parallel$ on each panel. For the transverse polarization, the φ-dependence becomes pronounced at $K_\perp \gtrsim \hbar/a_m \approx 30$ a.u. The upper and lower dashed curves correspond to the largest and smallest possible values of $\sigma_\perp(\varphi)$, at $\varphi = 0$ and $\varphi = 90°$, respectively, because the transversely polarized photons "see" the largest transverse size of the atom (stretched perpendicular to $\boldsymbol{K}_\perp$) when they propagate along $\boldsymbol{K}_\perp$ and the smallest size when they propagate transverse to $\boldsymbol{K}_\perp$. The φ-dependence between these two extremes, illustrated in Figure 4, is described by the formula

$$\sigma_\perp(\varphi) = \frac{\sigma_+ + \sigma_-}{2} + A \cos 2\varphi \, . \qquad (9)$$

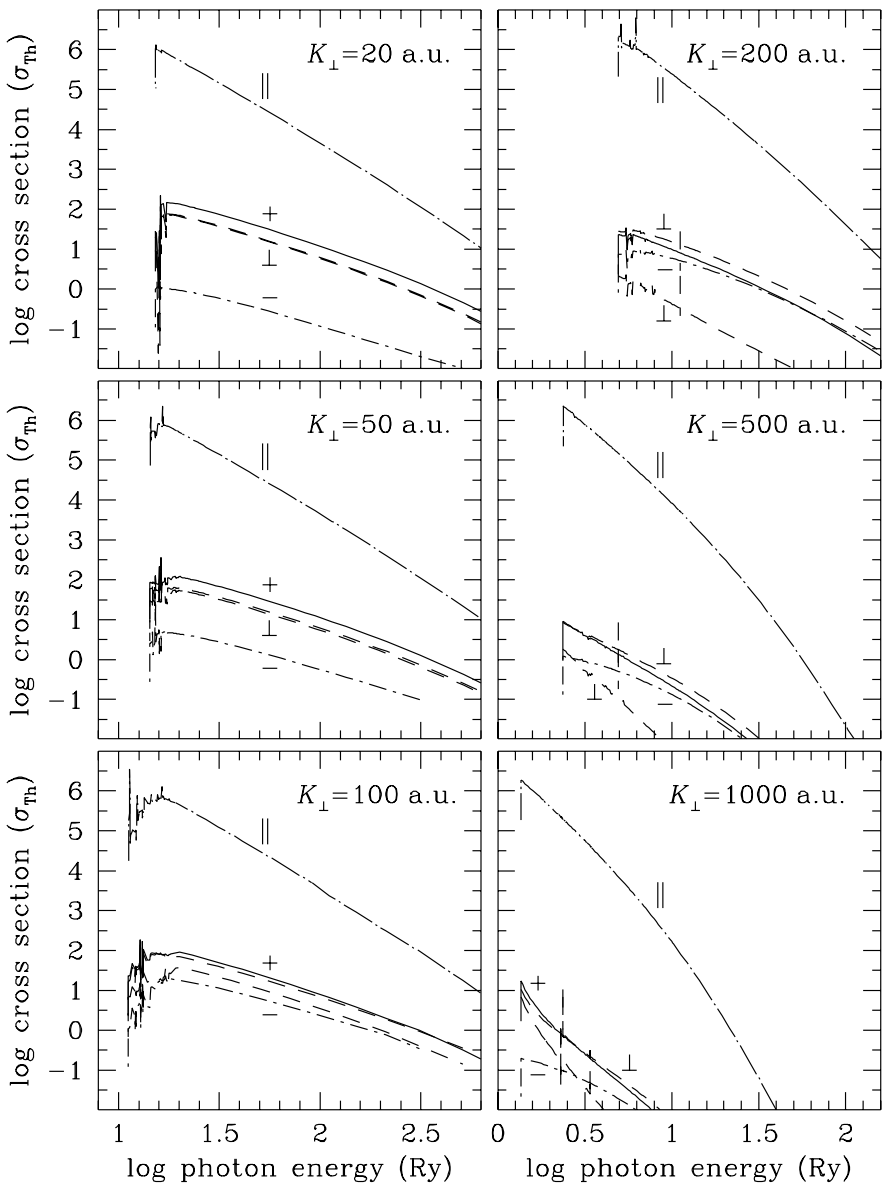

FIG. 3.—Photoionization cross sections of the ground-state H atom moving with various $K_\perp$ in a magnetic field $B = 2.35 \times 10^{12}$ G. Solid and dot-dashed lines correspond to the right (+) and left (−) circular polarizations of photons propagating along the magnetic field; dot–long-dashed and dashed lines correspond to the linear polarizations parallel (∥) and perpendicular (⊥) to the field for the transverse propagation. The upper and lower dashed curves are for the wavevector parallel to and perpendicular to the transverse component of the generalized momentum, respectively.

Note that in the absence of coupling of different s-channels the amplitude A in equation (9) would equal $(\sigma_+\sigma_-)^{1/2}$, which is always greater than the actual value of A calculated numerically.

The curve corresponding to $E_f = 1.1$ Ry in Figure 4 is significantly higher than that corresponding to $E_f = 1$ Ry because the ionization channel $s' = 1$ opens at $E_f = \hbar\omega_{cp} = 1.089$ Ry, where $\omega_{cp} = (m_e/m_p)\omega_c$ is the proton cyclotron frequency. The curve corresponding to $E_f = 2$ Ry goes much higher than the other curves because it falls on a slope of a Beutler-Fano resonance. Such resonances are most prominent at $K_\perp \sim K_c$ (see Fig. 3) because of the violation of the s-adiabatic approximation in this range of the transverse generalized momenta. Nevertheless, these peaks remain very narrow. Figure 5 presents some autoionization widths Γ_a calculated according to equations (14) and (15) of PPV97 (with obvious generalization to the case of moving atoms). The left panel shows the widths of the tightly-bound states $s = 1$–4 that enter the continuum at $K_\perp \approx 1200$, 560, 340, and 237 a.u., respectively (see Fig. 1). Because of the similarity of the effective potentials related to different s values, the jumps of the curves corresponding to opening of additional autoionization channels occur at nearly these same values of $K_\perp$. The hydrogen-like levels of the ($s = 1$) manifold (*right*, Fig. 5) belong to the continuum at any $K_\perp$. The autoionization widths vanish at $K_\perp \ll K_c$ and at $K_\perp \gg K_c$ the wave functions are cylindrically symmetric in these limits.

3.2. *Absorption by Atoms in Thermal Equilibrium*

The bound-free absorption coefficient for a hydrogen gas of given temperature and density is proportional to the photoionization cross section $\sigma_{\kappa\to\kappa'}(\boldsymbol{K}_\perp)$ folded with $N_\kappa(\boldsymbol{K})$, the distribution of the number density of atoms in the initial

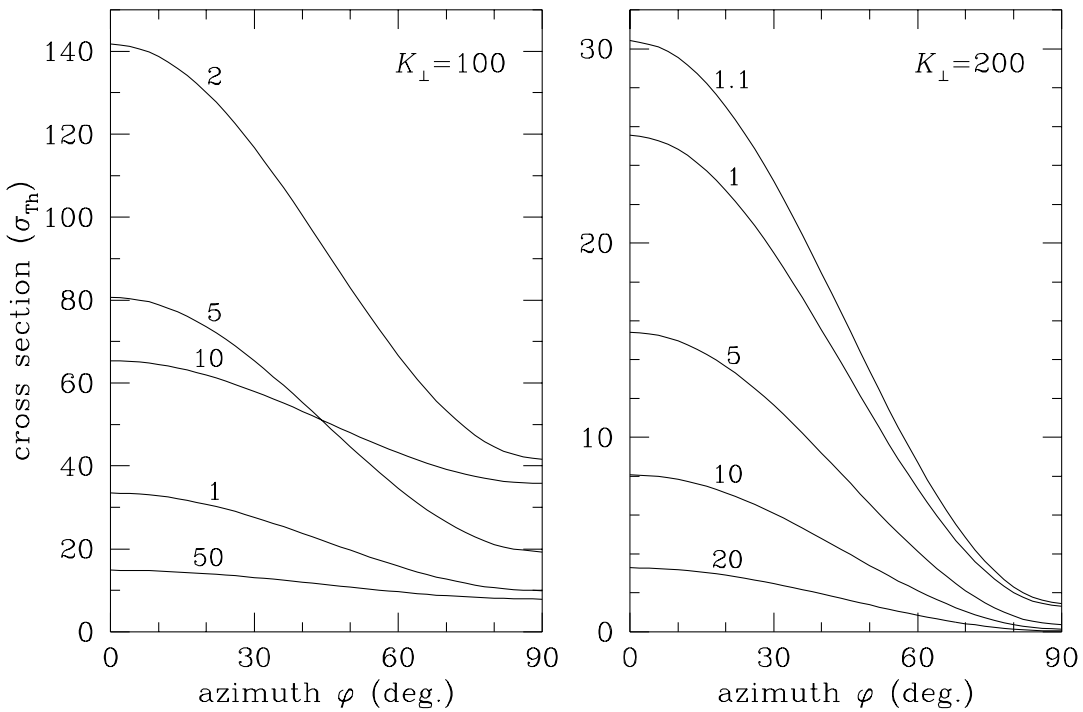

FIG. 4.—Angular dependence of the photoionization cross section $\sigma_\perp$ of a ground-state H atom moving with $K_\perp = 100$ or 200 a.u. in the magnetic field $B = 2.35 \times 10^{12}$ G. The wavevector and polarization direction are perpendicular to the magnetic field. Numbers near the curves indicate energies E_f of the final state (in Ry).

state. Since the level energy $E_\kappa(K_\perp)$ tends to a constant value at $K_\perp \to \infty$, the normalization integral for the Boltzmann distribution $N_\kappa(\boldsymbol{K}) \propto \exp\,[-E_\kappa(K_\perp)/k_B\,T]$ diverges. The divergence is eliminated if nonideality of the gas is taken into account. At high $K_\perp$, the binding energies become small and atomic sizes become large; hence the atom can be easily destroyed by surrounding particles, so that very high values of $K_\perp$ should not contribute to the corresponding integrals. In order to allow for this effect, we use the occupation probability formalism, described in detail by Hummer & Mihalas (1988) and generalized to the case of the $K_\perp$-dependent atomic structure by PP95. Fol-

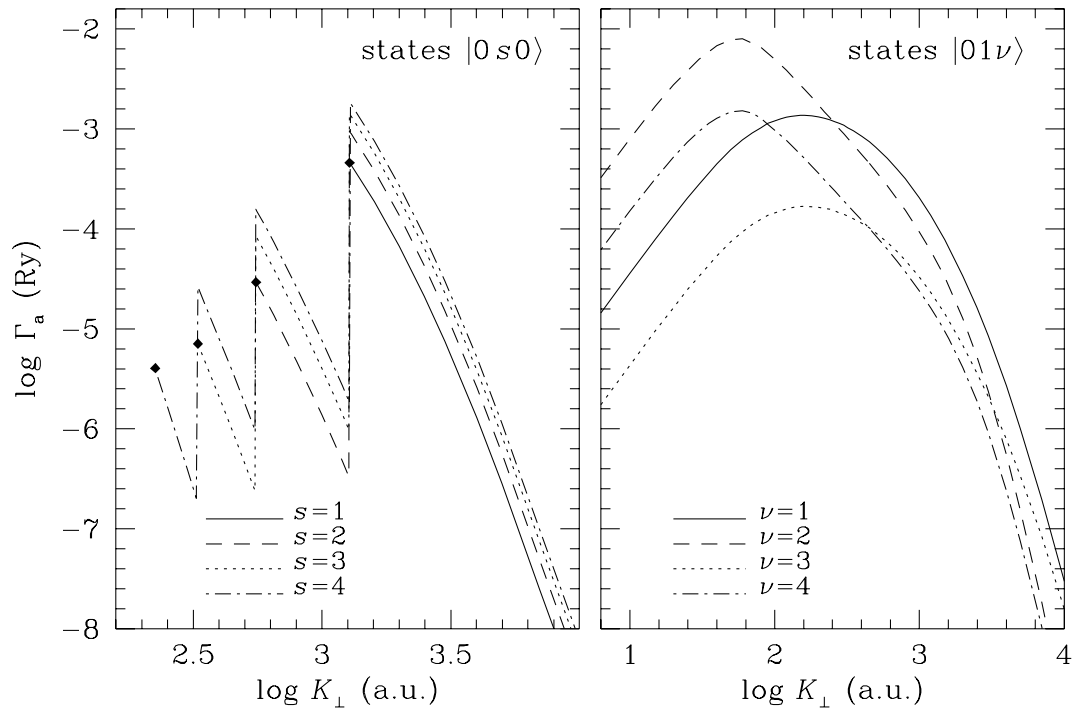

FIG. 5.—Autoionization widths of several tightly-bound (*left*) and hydrogen-like (*right*) atomic resonances as function of $K_\perp$ for $B = 2.35 \times 10^{12}$ G. Each curve in the left panel starts from the point where the corresponding state enters the continuum.

lowing this approach, we write

$$N_\kappa(\boldsymbol{K}) \propto w_\kappa(K_\perp) \exp\left[-E_\kappa(K_\perp)/k_B T\right], \quad (10)$$

where $w_\kappa(K_\perp)$ is the occupation probability, equal to the fraction of atoms (in the specified state $|\kappa, \boldsymbol{K}\rangle$) that essentially preserve quantum-mechanical (and especially optical) properties of an isolated atom. We estimate $w_\kappa(K_\perp)$ according to equation (14) of PP95 based on the quantum-mechanical atomic sizes calculated by P94. A rapid decrease of $w_\kappa(K_\perp)$ at $K_\perp \gtrsim \gamma\hbar/a_B$ (see Fig. 3 of PP95) limits contribution from atoms with large generalized momenta and provides convergence of integrals over $K_\perp$.

Since the threshold energies decrease with increasing $K_\perp$, folding the photoionization cross sections with $N_\kappa(K_\perp)$ leads to redward broadening of the photoionization edges with a typical width $\Gamma_M \sim k_B T$ (PM93). It has been shown by PM93 and PP95 that the "magnetic width" is much greater than the Doppler and (impact) collisional widths under typical conditions of NS atmospheres. In this paper we take full account of the magnetic broadening and neglect other broadening mechanisms.

The averaged photoionization cross sections for atoms on the ground level are shown in Figure 6 for two values of the temperature T. For comparison, we show also cross sections for the bound-bound (b-b) transitions from the ground level (PP95). Both the b-b and bound-free (b-f) averaged cross sections are corrected for the stimulated emission, i.e., multiplied by $(1 - \exp[-\hbar\omega/k_B T])$. For the circular polarizations, the b-b and b-f transitions dominate in different (adjacent) spectral ranges—the low-energy b-f component, arising from the decentered states (Fig. 3), turns out to be much weaker than the b-b component in the same energy range. For $\sigma_\parallel$, the same is the case at $\log T = 5.2$ but not at $\log T = 5.8$. In the latter case, the low-energy b-f component dominates the absorption spectrum except at very low energies $\hbar\omega \lesssim 40$ eV.

The peak of σ_+ in the right panel of Figure 6 at $\hbar\omega \approx 15$ eV and the corresponding peaks of the b-b curves arise near the proton cyclotron frequency ω_{cp}, around which the transitions of strongly decentered atoms are concentrated (PP95).

Figure 7 demonstrates the effect of density on the averaged photoionization cross sections. The low-energy component rapidly decreases with increasing ρ because the decentered atoms, because of their large sizes, are more easily destroyed by the plasma microfields. The growth of the high-energy component noticeable at higher T is explained by the relative increase of the number of centered atoms when the decentered atoms are destroyed. It should be noted that at high densities one more effect, broadening of the photoionization edges by quasi-static interactions with surrounding particles, may become important. As the density grows, highly excited bound states become randomly disturbed by the surroundings and form a quasi-continuum. This process results in continuous photon absorption below the undisturbed photoionization threshold (e.g., Däppen, Anderson, & Mihalas 1987). These "bound–quasi-free" transitions require a separate treatment and are not treated in the present paper.

Figure 8 shows the effects of T and B on the photoabsorption spectral shapes. With growing T, the low-energy components significantly increase and the high-energy components of $\sigma_\parallel$ and σ_+ decrease slightly because the decentered states become more populated. At lower T, the high-energy component of σ_- grows with T linearly as

$$\sigma_- \approx \frac{\hbar\omega_{cp} k_B T}{2\epsilon^2_{000,010}} \sigma_+ , \quad (11)$$

in accordance with the result of PM93 obtained in the perturbation regime ($\epsilon_{000,010}$ is the energy of the main b-b transition for the right polarization—e.g., $\epsilon_{000,010} \simeq 70$ eV

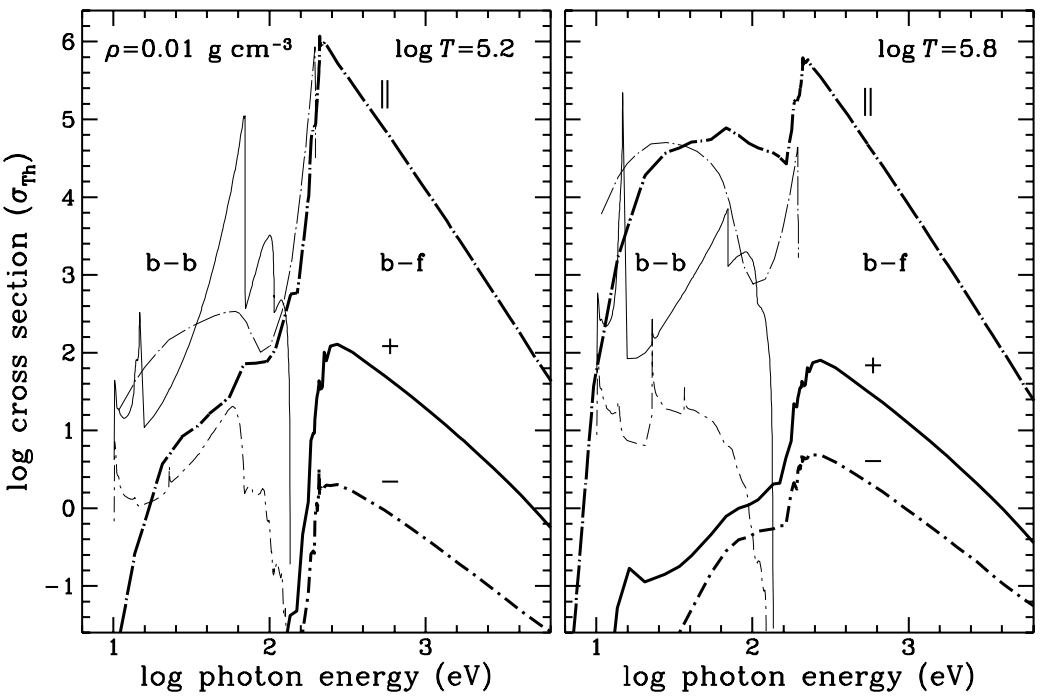

FIG. 6.—Photoionization cross sections (*heavy lines*) for three polarizations (indicated as in Fig. 3), averaged over the thermal distribution of atoms at magnetic field $B = 2.35 \times 10^{12}$ G, density $\rho = 0.01$ g cm^{-3}, and temperatures $T = 10^{5.2}$ K and $10^{5.8}$ K. Light lines represent cross sections arising from bound-bound transitions (PP95).

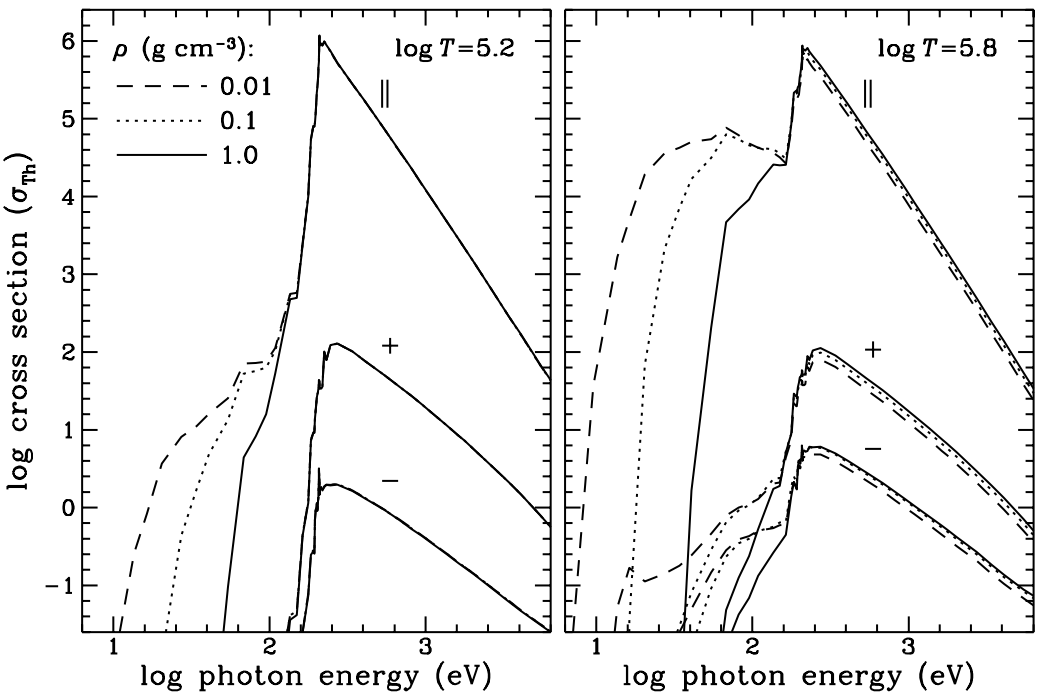

FIG. 7.—Averaged photoionization cross sections for three polarizations, at $B = 2.35 \times 10^{12}$ G, $\rho = 0.01$, 0.1, or 1 g cm^{-3}, and $T = 10^{5.2}$ K or $T = 10^{5.8}$ K

for $\gamma = 1000$). At higher T, the growth of σ_- decelerates because of the decreasing fraction of the centered states and because of nonperturbative effects.

At higher B, the proton cyclotron resonance discussed above for σ_+ becomes stronger. Because of the approximate similarity of the energy spectra related to different s-manifolds (see Fig. 1), the individual Beutler–Fano resonances, although smoothed by the thermal averaging, are collected together into regularly spaced peaks. Such peaks corresponding to four proton cyclotron harmonics are indicated by arrows for σ_- at $\gamma = 3000$ in Figure 8. At high densities, the peaks can be further smoothed by interaction with surrounding particles.

4. CONCLUSIONS

The results presented here provide, together with the results of PP95 on the bound-bound transitions, a basis for calculations of realistic opacities of NS atmospheres. To find the opacities, one should add transitions from excited atomic levels, which is straightforward. More difficult are the problems of ionization equilibrium in dense, nonideal plasmas and the closely related problem of the nonideality effects on the bound-free transitions (including transitions to the quasi-free states below the unperturbed photoionization threshold). Finally, polarizations of the normal modes for any frequency and direction of propagation should be found in order to solve the radiative transfer equations. Bulik & Pavlov (1996) have described how these polarizations can be calculated if the basic cross sections $\sigma_\pm$ and $\sigma_\parallel$ are known.

Our results show that atomic motion in strong magnetic fields drastically changes both the bound-bound and bound-free opacities. In particular, it considerably broadens the spectral lines and photoionization edges (with a typical magnetic width $\sim k_B T$), gives rise to additional absorption at low frequencies due to decentered atoms, and opens new transition channels forbidden for atoms at rest. These unusual properties of the spectral opacities alter the structure of the NS atmospheres and manifest themselves in the spectra and light curves of radiation emergent from the NS surface layers.

The authors are grateful to Victor Bezchastnov and Joseph Ventura for fruitful discussions, and to Cole Miller and the referee, Tomek Bulik, for useful remarks. This work was partially supported through NASA grant NAG 5-2807, INTAS grant 94-3834, RBRF grant 96-02-16870a, and DFG–RBRF grant 96-02-00177G. A. Y. P. gratefully acknowledges the hospitality of Joseph Ventura at the University of Crete, Gilles Chabrier at the École Normale Supèrieure de Lyon, and Chris Pethick at Nordita, where a part of this work was done.

APPENDIX

INTERACTION MATRIX ELEMENTS

Velocity and length representations of the operator of interaction of a moving hydrogen atom with radiation have been derived by BP94. Here we employ the velocity representation as the simpler one. KVH96 have noted that the interaction of the radiation field with the electron spin should be taken into account. It has been found by PPV97 that the spin term almost does not change the cross sections at all at energies below 10 keV. Nevertheless, we include this term for the sake of generality,

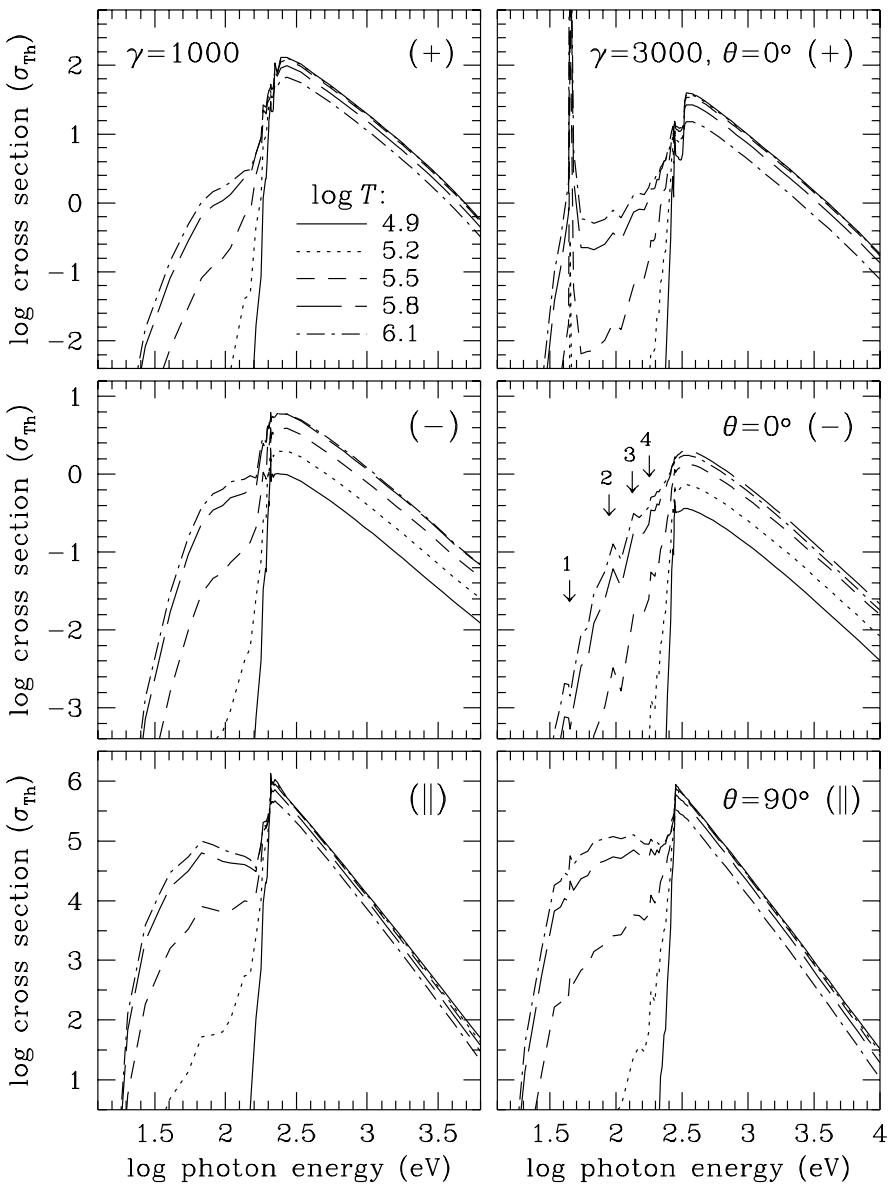

FIG. 8.—Averaged photoionization cross sections for the right (*top*), left (*middle*), and longitudinal (*bottom*) polarizations for $\rho = 0.1$ g cm^{-3}, $B = 2.35 \times 10^{12}$ G and 7×10^{12} G (*left* and *right*, respectively), and various temperatures.

neglecting the terms responsible for the spin-flip transitions (Schmitt et al. 1981), which are strictly forbidden at the photon energies considered, which are below $\hbar\omega_c$.

In the conventional representation of the wave functions, equation (A6) of BP94 yields, for the dimensionless interaction operator $\hat{M}$,

$$(2a_B)^{-1}\hat{M} = \exp\left(i\frac{m_p}{m_H}\boldsymbol{q}\cdot\boldsymbol{r}\right)\left[\left(\frac{\boldsymbol{\pi}}{\hbar}+\frac{m_e}{m_H}\frac{\boldsymbol{K}}{\hbar}+\frac{\boldsymbol{q}}{2}\right)\cdot\boldsymbol{e}-\frac{i}{2}(\boldsymbol{q}\times\boldsymbol{e})_z\right]+\left(\frac{m_e}{m_p}\frac{\boldsymbol{\Pi}}{\hbar}-\frac{m_e}{m_H}\frac{\boldsymbol{K}}{\hbar}\right)\cdot\boldsymbol{e}\,, \tag{A1}$$

where $\boldsymbol{q}$ is the photon wavevector, $\boldsymbol{e}$ is its polarization vector, and negligibly small terms $\sim(m_e/m_p)q$ are omitted. Here $\boldsymbol{r} = \boldsymbol{r}_e - \boldsymbol{r}_p$ is the relative coordinate and $\boldsymbol{\pi}$ and $\boldsymbol{\Pi}$ are the electron and proton kinetic momentum operators

$$\boldsymbol{\pi} = \boldsymbol{p} + \frac{e}{2c}\boldsymbol{B}\times\boldsymbol{r}\,, \tag{A2a}$$

$$\boldsymbol{\Pi} = \boldsymbol{p} - \frac{e}{2c}\boldsymbol{B}\times\boldsymbol{r}\,. \tag{A2b}$$

Their cyclic components act on the Landau states as

$$\pi_\pm|ns\rangle_\perp = \mp\frac{i\hbar}{a_m}\sqrt{n_*}\,|n\pm1, s\mp1\rangle_\perp\,, \tag{A3a}$$

$$\Pi_{\pm}\,|\,ns\rangle_{\perp} = \mp\frac{i\hbar}{a_m}\sqrt{n_* + s}\,|\,n,\, s \mp 1\rangle_{\perp}\,, \tag{A3b}$$

where $n_* = n + 1$ and $n_* = n$ for the right (+) and left (−) components, respectively. If the full-shift representation, $\eta' = 1$, is used for the final state, and an arbitrary shift parameter η is used for the initial state, then, according to equation (A15) of BP94,

$$\hat{M} = \frac{2\hbar}{e^2}\left\{\exp\left[-\frac{i}{2}\frac{m_p - m_e}{m_{\rm H}}(1-\eta)\boldsymbol{K}\cdot\boldsymbol{r}_{\perp}\right]\right\}\left[\left[\boldsymbol{e}\cdot\left\{\boldsymbol{F}_e\exp\left[i\left(\frac{\boldsymbol{q}\cdot\boldsymbol{r}}{2} - q_z z\right)\right] - \boldsymbol{F}_p\exp\left[-i\eta\boldsymbol{r}_c\cdot\boldsymbol{q} - \frac{i\boldsymbol{q}\cdot\boldsymbol{r}_{\perp}}{2}\right]\right\}\right]\right], \tag{A4}$$

where $\boldsymbol{r} = \boldsymbol{r}_e - \boldsymbol{r}_p - \eta\boldsymbol{r}_c$. Once again, the terms $\sim qm_e/m_p$ are omitted. The components of the vector operators $\boldsymbol{F}_e$ and $\boldsymbol{F}_p$ are

$$F_{e+} = \frac{\pi_+}{m_e} + (1-\eta)\frac{K_+}{m_{\rm H}} + \frac{\hbar q_+}{m_e}\,, \tag{A5a}$$

$$F_{e-} = \frac{\pi_-}{m_e} + (1-\eta)\frac{K_-}{m_{\rm H}}\,, \tag{A5b}$$

$$F_{ez} = \frac{1}{m_e}\left(p_z + \frac{\hbar q_z}{2}\right), \tag{A5c}$$

$$F_{p\pm} = \frac{\Pi_{\pm}}{m_p} - (1-\eta)\frac{K_{\pm}}{m_{\rm H}}\,, \tag{A5d}$$

$$F_{pz} = \frac{p_z}{m_p}\,. \tag{A5e}$$

In order to proceed with equation (8), we need to calculate the transverse matrix elements $\langle n's'\eta'\,|\,\hat{M}\,|\,ns\eta\rangle_{\perp}$. In the particular case of the dipole approximation ($q \to 0$), such a calculation has been performed by BP94. In the general case, we use the following result obtained with the same operator technique as in BP94:

$$\left\langle n's'\eta',\, \boldsymbol{K}_{\perp} + \boldsymbol{q}_{\perp}\right|\exp\left[-\frac{i}{2}\frac{m_p - m_e}{m_{\rm H}}(\eta' - \eta)Kr_{\perp} + \frac{i\tilde{q}r_{\perp}}{2}\right]\left|ns\eta,\, \boldsymbol{K}_{\perp}\right\rangle_{\perp} = J_{nn'}(\xi_e)J_{n+s,n'+s'}(\xi_p)\,, \tag{A6}$$

where $\tilde{\boldsymbol{q}}$ is arbitrary,

$$\xi_e = -ia_m\left[\frac{m_e}{m_{\rm H}}(\eta' - \eta)K_+/\hbar + \frac{(\tilde{q}_+ + \eta' q_+)}{2}\right], \tag{A7a}$$

$$\xi_p = -ia_m\left[\frac{m_p}{m_{\rm H}}(\eta' - \eta)K_-/\hbar - \frac{(\tilde{q}_- - \eta' q_-)}{2}\right], \tag{A7b}$$

and

$$J_{nn'}(|\,\xi\,|\,e^{i\varphi}) = e^{i(n-n')\varphi}I_{nn'}(|\,\xi\,|^2)\,, \tag{A8}$$

with $I_{nn'}$ a Laguerre function (Sokolov & Ternov 1968).

Using equations (A4), (A3a), (A3b), and (A6) for $\eta' = 1$, and neglecting an insignificant common phase, we finally arrive at the expression for the interaction matrix element (8):

$$\langle f\,|\,\hat{M}\,|\,i\rangle = 2\sqrt{\gamma}\sum_{n's'ns}\left[e_+ M^{(-)}_{n's'ns} + e_- M^{(+)}_{n's'ns} + e_z M^{(z)}_{n's'ns}\right], \tag{A9}$$

where

$$\begin{aligned} M^{(-)}_{n's'ns} = &-\left[\sqrt{n}J_{n-1,n'}(\xi_{e,+}) + \zeta_{e,-}J_{nn'}(\xi_{e,+})\right]J_{n+s,n'+s'}(\xi_{p,+})\mathscr{Z}^{(e)}_{n's'ns} \\ &-\frac{m_e}{m_p}\exp\left(-i\eta\boldsymbol{r}_c\cdot\boldsymbol{q}\right)\left[\sqrt{n+s+1}J_{n+s+1,n'+s'}(\xi_{p,-}) - \zeta_{p,-}J_{n+s,n'+s'}(\xi_{p,-})\right] \\ &\times J_{nn'}(\xi_{e,-})\mathscr{Z}^{(p)}_{n's'ns}\,, \end{aligned} \tag{A10a}$$

$$\begin{aligned} M^{(+)}_{n's'ns} = &\left[\sqrt{n+1}J_{n+1,n'}(\xi_{e,+}) - \zeta_{e,+}J_{nn'}(\xi_{e,+})\right]J_{n+s,n'+s'}(\xi_{p,+})\mathscr{Z}^{(e)}_{n's'ns} \\ &+\frac{m_e}{m_p}\exp\left(-i\eta\boldsymbol{r}_c\cdot\boldsymbol{q}\right)\left[\sqrt{n+s}J_{n+s+1,n'+s'}(\xi_{p,-}) + \zeta_{p,+}J_{n+s,n'+s'}(\xi_{p,-})\right] \\ &\times J_{nn'}(\xi_{e,-})\mathscr{Z}^{(p)}_{n's'ns}\,, \end{aligned} \tag{A10b}$$

$$\begin{aligned} M^{(z)}_{n's'ns} = &\left[\tilde{\mathscr{Z}}^{(e)}_{n's'ns} + \frac{i}{2}a_m q_z\mathscr{Z}^{(e)}_{n's'ns}\right]J_{nn'}(\xi_{e,+})J_{n+s,n'+s'}(\xi_{p,+}) \\ &+\frac{m_e}{m_p}\exp\left(-i\eta\boldsymbol{r}_c\cdot\boldsymbol{q}\right)\left[\tilde{\mathscr{Z}}^{(p)}_{n's'ns} - \frac{i}{2}a_m q_z\mathscr{Z}^{(p)}_{n's'ns}\right]J_{nn'}(\xi_{e,-})J_{n+s,n'+s'}(\xi_{p,-})\,. \end{aligned} \tag{A10c}$$

In these equations

$$\zeta_{e,+} = -\frac{ia_m}{\hbar}\left[\frac{m_e}{m_{\rm H}}(1-\eta)K_+ + \hbar q_+\right], \tag{A11a}$$

$$\zeta_{e,-} = -\frac{ia_m}{\hbar}\frac{m_e}{m_{\rm H}}(1-\eta)K_- , \tag{A11b}$$

$$\zeta_{p,\pm} = -\frac{ia_m}{\hbar}\frac{m_p}{m_{\rm H}}(1-\eta)K_\pm , \tag{A11c}$$

$\xi_{e,\pm}$ and $\xi_{p,\pm}$ are given by equations (A7) with $\eta' = 1$ and $\tilde{\boldsymbol{q}} = \pm\boldsymbol{q}$, respectively, and the factors

$$\mathscr{Z}^{(e)}_{n's'ns} = \langle n's', f \,|\, e^{iq_z z} \,|\, ns\eta, i\rangle_{\parallel} , \qquad \mathscr{Z}^{(p)}_{n's'ns} = \langle n's', f \,|\, ns\eta, i\rangle_{\parallel} , \tag{A12a}$$

$$\tilde{\mathscr{Z}}^{(e)}_{n's'ns} = \left\langle n's', f \left| e^{iq_z z} a_m \frac{\partial}{\partial z} \right| ns\eta, i \right\rangle_{\parallel} , \qquad \tilde{\mathscr{Z}}^{(p)}_{n's'ns} = \left\langle n's', f \left| a_m \frac{\partial}{\partial z} \right| ns\eta, i \right\rangle_{\parallel} \tag{A12b}$$

are the longitudinal matrix elements, which can be numerically evaluated.

We have presented the result for $\eta' = 1$. For arbitrary η', the matrix elements are obtained in analytic form using equation (A15) of BP94 and our equations (A6), (A7) with $\tilde{\boldsymbol{q}} = [2m_e + \eta'(m_p - m_e)]\boldsymbol{q}/m_{\rm H}$ and $\tilde{\boldsymbol{q}} = -[2m_p + \eta'(m_e - m_p)]\boldsymbol{q}/m_{\rm H}$. The result is a straightforward generalization of equations (A10).

REFERENCES

Bezchastnov, V. G., & Potekhin, A. Y. 1994, J. Phys. B, 27, 3349 (BP94)
Bulik, T., & Pavlov, G. G. 1996, ApJ, 469, 373
Burkova, L. A., Dzyaloshinskii, I. E., Drukarev, G. F., & Monozon, B. S. 1976, Sov. Phys.—JETP, 44, 276
Däppen, W., Anderson, L. S., & Mihalas, D. 1987, ApJ, 319, 195
Gnedin, Yu. N., Pavlov, G. G., & Tsygan, A. I. 1974, Sov. Phys.—JETP, 39, 301
Gorkov, L. P., & Dzyaloshinskii, I. E. 1968, Sov. Phys.—JETP, 26, 449
Hummer, D. G., & Mihalas, D. 1988, ApJ, 331, 794
Johnson, B. R., Hirschfelder, J. O., & Yang, K.-H. 1983, Rev. Mod. Phys., 55, 109
Kopidakis, N., Ventura, J., & Herold, H. 1996, A&A, 308, 747 (KVH96)
Miller, M. C., & Neuhauser, D. 1991, MNRAS, 253, 107
Ögelman, H. 1995, in The Lives of the Neutron Stars, eds. M. A. Alpar, Ü. Kiziloğlu, & J. van Paradijs (Dordrecht: Kluwer), 101
Pavlov, G. G., & Mészáros, P. 1993, ApJ, 416, 752 (PM93)
Pavlov, G. G., Shibanov, Yu. A., Zavlin, V. E., & Meyer, R. D. 1995, in The Lives of the Neutron Stars, eds. M. A. Alpar, Ü. Kiziloğlu, & J. van Paradijs (Dordrecht: Kluwer), 71
Pavlov, G. G., & Potekhin, A. Y. 1995, ApJ, 450, 883 (PP95)
Pethick, C. J. 1992, Rev. Mod. Phys., 64, 1133
Potekhin, A. Y. 1994, J. Phys. B, 27, 1073 (P94)
Potekhin, A. Y., & Pavlov, G. G. 1993, ApJ, 407, 330 (PP93)
Potekhin, A. Y., Pavlov, G. G., & Ventura, J. 1997, A&A, 317, 618 (PPV97)
Romani, R. W. 1987, ApJ, 313, 718
Schmitt, W., Herold, H., Ruder, H., & Wunner, G. 1981, A&A, 94, 194
Sokolov, A. A., & Ternov, I. M. 1968, Synchrotron Radiation (Berlin: Academic)
Ventura, J., Herold, H., Ruder, H., & Geyer, F. 1992, A&A, 261, 235
Vincke, M., Le Dourneuf, M., & Baye, D. 1992, J. Phys. B, 25, 2787
Wunner, G., Ruder, H., Herold, H., & Schmitt, W. 1983, A&A, 117, 156